LETTER

https://doi.org/10.1038/s41586-018-0107-1

Dynamic band-structure tuning of graphene moiré superlattices with pressure

Matthew Yankowitz[1], Jeil Jung[2], Evan Laksono[3,4], Nicolas Leconte[2], Bheema L. Chittari[2], K. Watanabe[5], T. Taniguchi[5], Shaffique Adam[3,4,6], David Graf[7] & Cory R. Dean[1]*

Heterostructures can be assembled from atomically thin materials by combining a wide range of available van der Waals crystals, providing exciting possibilities for designer electronics[1]. In many cases, beyond simply realizing new material combinations, interlayer interactions lead to emergent electronic properties that are fundamentally distinct from those of the constituent layers[2]. A critical parameter in these structures is the interlayer coupling strength, but this is often not easy to determine and is typically considered to be a fixed property of the system. Here we demonstrate that we can controllably tune the interlayer separation in van der Waals heterostructures using hydrostatic pressure, providing a dynamic way to modify their electronic properties. In devices in which graphene is encapsulated in boron nitride and aligned with one of the encapsulating layers, we observe that increasing pressure produces a superlinear increase in the moiré-superlattice-induced bandgap—nearly doubling within the studied range—together with an increase in the capacitive gate coupling to the active channel by as much as 25 per cent. Comparison to theoretical modelling highlights the role of atomic-scale structural deformations and how this can be altered with pressure. Our results demonstrate that combining hydrostatic pressure with controlled rotational order provides opportunities for dynamic band-structure engineering in van der Waals heterostructures.

Heterostructures fabricated by mechanical assembly of atomically thin van der Waals (vdW) crystals represent an exciting new paradigm in materials design. Owing to weak interlayer bonding, two-dimensional (2D) crystals with wide-ranging characteristics and composition—such as graphene, boron nitride (BN) and the transition metal dichalcogenides—can be readily mixed and matched, without the usual interfacial constraints of conventional crystal growth[3]. Moreover, atomic-scale crystalline alignment between the layers often plays a critical role in the resulting device characteristics, leading to additional and controllable degrees of freedom. For example, electronic coupling processes that are sensitive to momentum mismatch, such as interlayer tunnelling[4] or exciton binding[5], can be sensitively tuned by varying the rotational order. For crystals with closely matched lattice constants, moiré interference at zero-angle alignment can additionally result in long-range superlattice potentials, which in turn can lead to entirely new electronic device characteristics[6–14].

BN-encapsulated graphene provides a model example of the variety of electronic properties that can be realized on demand in a single type of vdW heterostructure. At large relative twist angles, BN acts as a featureless dielectric for graphene, minimizing coupling to extrinsic disorder but otherwise remaining effectively inert[15]. However, at small twist angle, coupling to the resulting moiré superlattice (MSL) profoundly alters the graphene band structure, giving rise to secondary Dirac cones at finite energy[6,16] while also modifying the Fermi velocity near the Dirac point[16]. As a consequence, several unusual electronic properties have been observed, such as density-dependent topological valley currents at zero magnetic field[11] and the fractal Hofstadter butterfly spectrum at high field[7–9]—recently identified as hosting integer and fractional Chern insulating states[14] and charge density waves[12,17]. Additionally, the MSL opens bandgaps at both the primary and secondary Dirac points of graphene, which are of particular interest for graphene-based digital logic.

Numerous techniques have been developed to control the rotational alignment in graphene/BN and related vdW heterostructures[7,12,13,18–21]. Equally important is the spacing between the layers, which dictates the magnitude of interlayer interactions. Little experimental work has

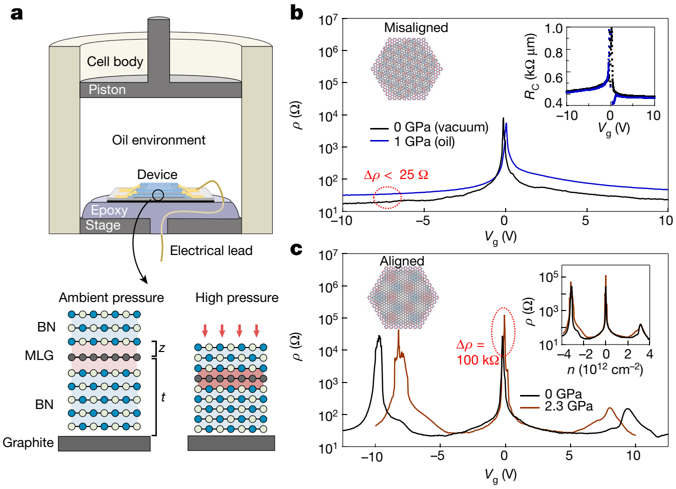

Fig. 1 | Experiment schematic and transport characterization under pressure. a, Top, cartoon of the piston-cylinder pressure cell. The sample is mounted inside a Teflon cup filled with oil. The pressure exerted on the sample is determined by the force applied to the piston. Electrical feedthroughs embedded in an epoxy junction enable in situ transport measurements. Bottom, schematic of the sample of graphene (MLG, monolayer graphene) encapsulated between two flakes of BN with a graphite gate. Neighbouring layers sit a distance z from one another. The distance between the top graphite layer and the graphene t sets the dielectric thickness. On the right, the same structure is shown under pressure, with each layer compressed towards its neighbour, decreasing both z and t and enhancing the interlayer electronic coupling (red hue). **b**, Resistivity of a misaligned device (device P2) in vacuum and at high pressure (1 GPa) in oil, exhibiting little pressure dependence. The contact resistance R_c (taken as the difference between the two- and four-terminal resistances) also exhibits virtually no dependence on pressure (inset). **c**, Resistivity of an aligned device (P1). The SDPs appear at different gate voltages as a function of pressure, but are perfectly aligned when plotted against n (inset). The PDP becomes noticeably more insulating with pressure, as highlighted in the red dashed oval. Cartoon insets in **b** and **c** show schematics of the moiré patterns that arise from the relative alignment of the graphene and BN. All measurements are taken at $B = 0$ T and $T = 2$ K.

---

[1]Department of Physics, Columbia University, New York, NY, USA. [2]Department of Physics, University of Seoul, Seoul, South Korea. [3]Centre for Advanced 2D Materials, National University of Singapore, Singapore, Singapore. [4]Department of Physics, Faculty of Science, National University of Singapore, Singapore, Singapore. [5]National Institute for Materials Science, Tsukuba, Japan. [6]Yale-NUS College, Singapore, Singapore. [7]National High Magnetic Field Laboratory, Tallahassee, FL, USA. *e-mail: cd2478@columbia.edu

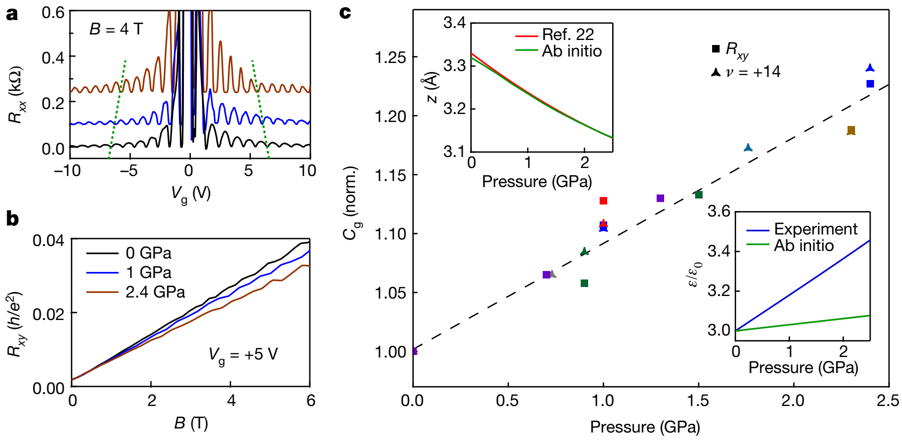

Fig. 2 | Modification of gate capacitance under pressure. **a**, Longitudinal resistance R_{xx} of device P2 at $B = 4$ T and $T = 2$ K. The green dotted lines track the same quantum Hall feature with pressure. Curves are vertically offset proportional to the pressure applied. **b**, R_{xy} as a function of pressure in the same device at $V_g = +5$ V. **c**, Gate capacitance C_g as a function of pressure, normalized to its value at 0 GPa for each device. Colours represent measurements on different devices. The square markers calculate C_g using n extracted from the low-field R_{xy}. The triangle markers use n extracted from the high-field dispersion of $\nu = 14$, where ν is the filling factor. Top inset, change in BN interlayer spacing per layer as a function of pressure predicted by LDA ab initio modelling (green curve). This almost exactly matches previous measurements by X-ray diffraction[22] (reproduced in the red curve). Bottom inset, he remaining increase in C_g with pressure is attributed to an enhancement of the BN dielectric constant ε, assuming $\varepsilon = 3$ at 0 GPa as taken from experiment (blue curve). The green curve shows the LDA ab initio modelling of bulk BN.

been done to characterize or control this parameter, which is often not well-known and is assumed to be invariable. Here we demonstrate that by applying hydrostatic pressure to BN-encapsulated graphene, we can decrease the interlayer spacing by more than 5%. At small rotation angles, the resulting increase in the effective MSL potential substantially modifies the electronic device characteristics. Most notably, with increasing pressure we observe a superlinear increase in the moiré-induced bandgap at the primary Dirac point (PDP)—nearly doubling over the pressure ranges studied—to yield the largest gap so far demonstrated in pristine monolayer graphene by 35%. By contrast, the gap at the secondary Dirac point (SDP) shows little change with pressure. This unexpected result provides new insight into the precise influence of the MSL on the graphene layer and suggests that in addition to electrostatic coupling, lattice-scale deformations play an important role. Our findings reveal that interlayer spacing in vdW heterostructures is an important and tunable degree of freedom that provides a new route to band-structure engineering.

Figure 1a shows a cartoon schematic of our experimental set-up. We fabricate BN-encapsulated graphene devices using the vdW assembly technique[3] and mount them into a piston-cylinder pressure cell with electrical feedthroughs, capable of reaching temperatures below 1 K and magnetic fields above 18 T. The sample space in the pressure cell is filled with oil which results in a uniform transfer of pressure to the sample (see Methods and Extended Data Fig. 1 for details). We first examine the effect of applying pressure on a misaligned heterostructure for which no MSL effects are present, and find that the oil environment and application of pressure have virtually no effect on the electronic properties of the graphene. Figure 1b shows low-temperature transport acquired from a misaligned device (>2° relative alignment) at zero magnetic field both in vacuum (with no oil) and under high pressure (1 GPa). The high-density resistance grows by a small amount, less than 25 Ω, with pressure in this device. Other similar devices showed no measurable change or even slightly decreasing resistance under pressure, indicating that the field effect mobility of the encapsulated

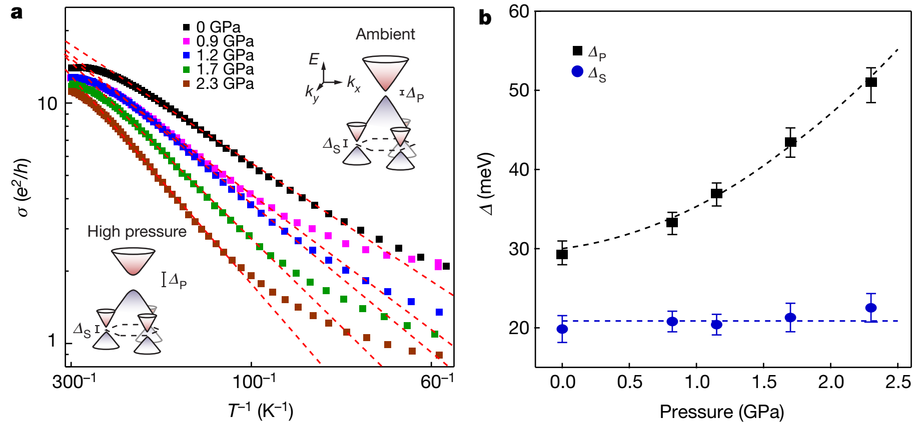

Fig. 3 | Bandgaps as a function of pressure. **a**, Arrhenius plot of the conductivity of the PDP as a function of inverse temperature for device P1 at various pressures. The slopes of the linear fits (red dotted lines) give the bandgap Δ at each pressure via $\sigma_{\mathrm{PDP}}(T) \propto \mathrm{e}^{-\Delta/(2kT)}$. Cartoon illustrations of the aligned graphene on BN band structure, indicating Δ_p and Δ_s and illustrating their dependence on pressure, are shown in the insets. Our model predicts SDPs at only one of the two valleys of the superlattice Brillouin zone. **b**, Bandgaps as a function of pressure. Δ_p grows with pressure, whereas Δ_s is relatively insensitive to pressure. Error bars in the gaps represent the uncertainty arising from determining the linear (thermally activated) regime for the fit (see Methods). The uncertainty in determining the pressure is smaller than the marker size. The dashed curves show the gaps predicted by the theoretical model using appropriately tuned deformations (see text).

device is largely insensitive to the application of pressure (see Extended Data Fig. 2). The PDP resistance is also not strongly modified, and there is no noticeable pressure dependence on the contact resistance (Fig. 1b inset).

Figure 1c shows similar transport measurements but acquired from an aligned MSL device. Under ambient pressure, the device shows excellent transport characteristics with moiré coupling evident by the appearance of two resistance peaks symmetrically located about the PDP at roughly $\pm 3.3 \times 10^{12}\,\mathrm{cm}^{-2}$, corresponding to a relative rotation angle of about 0.6°. Moreover, the large resistivities exceeding 25 kΩ at the PDP and SDP suggest sizeable bandgaps at those points in the band structure. Notably, as we apply high pressure up to 2.3 GPa, we find that the positions of the secondary peaks move symmetrically towards the PDP.

To understand this effect, we track the back gate capacitance per unit area $C_g = en/V_g = \varepsilon\varepsilon_0/t$, where e is the charge of the electron, ε is dielectric constant of BN, ε_0 is the vacuum permittivity, t is the thickness of the BN, V_g is the applied gate bias and n is the carrier density. We measure the density in two ways, both from the Hall effect and from magnetoresistance oscillations (Fig. 2a and b; see Methods). All devices exhibit a universal increase of C_g with pressure of roughly 9% per GPa, independent of their relative alignment (Fig. 2c), which must arise through a decrease in t and/or an increase in ε. To deconvolve the two, we have performed ab initio simulations of bulk BN multilayers under pressure, using the local density approximation (LDA) and find approximately 2.5% compression per GPa (green curve in the top inset of Fig. 2c), in good quantitative agreement with previous X-ray diffraction measurements[22] (reproduced in the red curve). The remaining increase in gate capacitance is therefore attributed to an increase in the dielectric constant of the BN of roughly 6% per GPa (blue curve in the bottom inset of Fig. 2c). Taken together, this suggests that pressure can sensitively tune both the interlayer spacing between layered 2D materials and their dielectric properties[23]. Returning to the transport measurements of the MSL device, we find that the three resistance peaks align exactly at all pressures when replotted against charge carrier density n (Fig. 1c inset), suggesting that although the graphene and BN layers move closer together, the relative rotation angle and moiré period remain fixed under pressure.

A second notable feature of the MSL transport is that the resistance at the PDP grows strongly with pressure, increasing by roughly 100 kΩ between 0 GPa and 2.3 GPa. We investigate the PDP response in more detail by measuring its temperature dependence. Figure 3a shows an Arrhenius plot of the PDP conductivity, σ_{PDP}, versus inverse temperature for various pressures, where for each pressure a linear fit to the thermally activated regime (red dashed lines) gives a measure of the activation gap (see Methods). The resulting PDP gap, Δ_p, is shown versus pressure in Fig. 3b (square markers). The gap is found to increase superlinearly with pressure, and is enhanced by nearly a factor of 2 at the highest pressure studied for the device presented here with relative rotation angle about 0.6°. We similarly measure the pressure dependence of the valence band SDP gap (Extended Data Fig. 3), Δ_s, plotted with filled circles in Fig. 3b. In contrast to the PDP gap, the SDP gap is nearly unresponsive to pressure. The insets of Fig. 3a schematically illustrate the inferred band-structure modifications with interlayer spacing, showing a growing Δ_p but a fixed Δ_s.

As a simple approximation, we may consider the increasing PDP gap with pressure to result from increasing MSL coupling owing to the decreasing interlayer spacing. In this case, we would expect that the SDP behaviour might respond in a similar way, and from this perspective its insensitivity to pressure is surprising. We note, however, that despite considerable effort[9,10,12,13,24–32], consensus is still lacking as to the exact origin of these bandgaps. Lattice-scale deformations (in-plane strains and out-of-plane corrugations) of the graphene layer are expected to play an important role[10,29–33], but the exact equilibrium structure of graphene in contact with BN remains poorly understood, including whether these deformations even exist in fully BN-encapsulated devices[10]. In an effort to understand the behaviour that we observe, we therefore first consider a rigid graphene lattice and examine the effects of pressure on the heterostructure by using a combination of ab initio and analytical models (see Methods and Supplementary Information). The interlayer electronic coupling between the graphene and BN, $V_0 = \tilde{V} e^{-\beta(z_0 - z_r)}$, is highly sensitive to pressure, with ab initio predictions indicating that the average interlayer spacing z_0 should decrease by about $0.07\,\text{Å}\,\mathrm{GPa}^{-1}$. Here $\tilde{V} \approx 18\,\mathrm{meV}$ is the interlayer electronic coupling, $z_r \approx 3.35\,\text{Å}$ is the equilibrium average interlayer spacing between the graphene and BN, and $\beta \approx 3.2\,\text{Å}^{-1}$ quantifies the rate of increase of interlayer coupling when the spacing is reduced. Generically, both Δ_p and Δ_s should scale proportionally to V_0 under applied pressure, but this is in stark contrast to our experimental observations in which Δ_s in particular exhibits little pressure dependence. Even at 0 GPa, a rigid model does not properly capture the experimentally observed hierarchy of the gaps, predicting a large Δ_s and a $\Delta_p \approx 0$ (Fig. 4a).

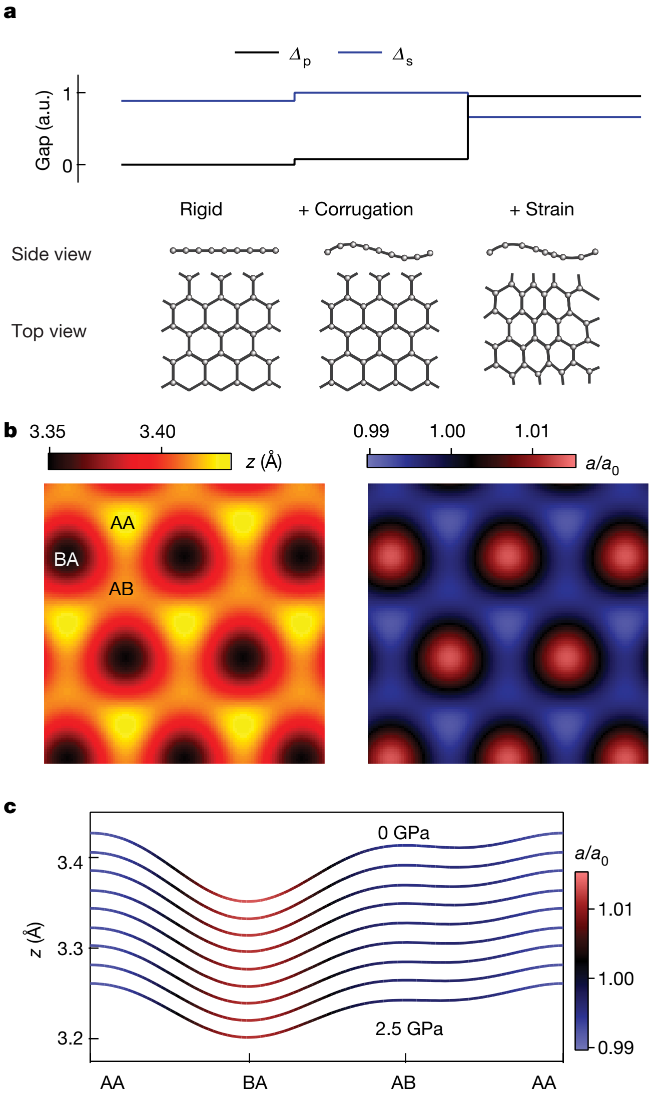

Fig. 4 | Modelling of the bandgaps. **a**, Relative contributions to Δ_p and Δ_s from lattice corrugations and strains. Strain is necessary to open a sizeable Δ_p, while deformations can substantially reduce Δ_s. Schematics of the graphene lattice structure for each case are illustrated below. **b**, Maps of the out-of-plane corrugations (left) and in-plane lattice strains (right) at 0 GPa used to model the gaps in Fig. 3b. **c**, Models for lattice corrugations through the high-symmetry points of the moiré as a function of pressure based on ab initio calculation inputs in BN-encapsulated graphene with one aligned interface. The left axis labels the atomic spacing between the BN and graphene lattices. The colour represents the magnitude of in-plane lattice strains needed to model the gaps in Fig. 3b.

Next we consider the potential role of atomic-scale graphene deformations. By considering realistic values of the graphene elastic deformation potential, our atomic structure models suggest that it is favourable for the graphene lattice both to corrugate out-of-plane and to be strained in-plane on the moiré scale to minimize the overall stacking potential with the BN substrate (Fig. 4b). These deformations break the sublattice symmetry of the graphene, resulting in a finite average mass term in the Hamiltonian which opens a sizeable Δ_p. There are also moiré-induced electrostatic potentials and pseudomagnetic fields that contribute to Δ_s in addition to the mass term. Including corrugations alone opens a small Δ_p at 0 GPa, but still does not recover the observed gap hierarchy of $\Delta_p > \Delta_s$ (Fig. 4a). By additionally including strains, we are able to recover the observed 0 GPa hierarchy of the gaps (Fig. 4a) as well as the superlinear increase in Δ_p and the flat Δ_s response with pressure. We find that we can quantitatively reproduce our experimental gap results with an analytical model for aligned graphene on BN which accounts for physically reasonable corrugations and strains consistent with predictions from ab initio modelling (dashed curves in Fig. 3b; see Methods and Supplementary Information for details of the model).

Although more experimental and theoretical work is necessary to understand the exact equilibrium structure of aligned graphene on BN, the varying evolution of the gaps with pressure directly rules out the possibility of a rigid graphene lattice in these structures, and moreover demonstrates that these gaps are of fundamentally different origin as the SDP cone is not a true replica of the PDP cone. This suggests the possibility of independent control over the magnitude of the two gaps, as well as other features of the moiré band structure and magnetoresponse, by selectively engineering specific lattice deformations. Additionally, sufficiently strong enhancement of the interlayer coupling could drive a phase transition to the fully commensurate (lattice-matched) stacking configuration[33], marked by the absence of a MSL but the emergence of strong sublattice-symmetry breaking in the graphene and a gap many times kT, where T is room temperature, at the Dirac point[26]. Even in the incommensurate configuration, extrapolating our results to 9 GPa (beyond which a phase transition in the crystal structure of the BN is expected) suggests that gaps as large as about 250 meV may be realized. This provides a potential new route to the long-pursued goal of engineering technologically relevant bandgaps in high-quality monolayer graphene. More generally, our results indicate that a wide variety of vdW heterostructure properties should be tunable by controlling the interlayer coupling strength with pressure, particularly those with emergent electronic properties driven by interlayer interactions. For example, sufficiently strong coupling to transition metal dichalcogenides with large spin–orbit coupling may drive topologically non-trivial gaps in graphene supporting a zero-field quantum spin Hall effect, and strong coupling to a vdW magnetic insulator may drive a quantum anomalous Hall effect. Even in simple vdW structures consisting of multilayers of the same material, fundamental features of the system such as the bandgap or the nature of properties such as superconductivity or magnetism scale with the interlayer coupling. Our demonstration of the tunability of interlayer interactions suggests that a wide variety of new device phenomena may now become experimentally accessible in 2D vdW structures.

Online content

Any Methods, including any statements of data availability and Nature Research reporting summaries, along with any additional references and Source Data files, are available in the online version of the paper at https://doi.org/10.1038/s41586-018-0107-1.

Received: 21 October 2017; Accepted: 14 February 2018;
Published online 16 May 2018.

1. Geim, A. K. & Grigorieva, I. V. Van der Waals heterostructures. *Nature* **499**, 419–425 (2013).
2. Novoselov, K. S., Mishchenko, A., Carvalho, A. & Castro Neto, A. H. 2D materials and van der Waals heterostructures. *Science* **353**, aac9439 (2016).
3. Wang, L. et al. One-dimensional electrical contact to a two-dimensional material. *Science* **342**, 614–617 (2013).
4. Mishchenko, A. et al. Twist-controlled resonant tunnelling in graphene/boron nitride/graphene heterostructures. *Nat. Nanotech.* **9**, 808–813 (2014).
5. Yu, H., Wang, Y., Tong, Q., Xu, X. & Yao, W. Anomalous light cones and valley optical selection rules of interlayer excitons in twisted heterobilayers. *Phys. Rev. Lett.* **115**, 187002 (2015).
6. Yankowitz, M. et al. Emergence of superlattice Dirac points in graphene on hexagonal boron nitride. *Nat. Phys.* **8**, 382–386 (2012).
7. Ponomarenko, L. A. et al. Cloning of Dirac fermions in graphene superlattices. *Nature* **497**, 594–597 (2013).
8. Dean, C. R. et al. Hofstadter's butterfly and the fractal quantum Hall effect in moiré superlattices. *Nature* **497**, 598–602 (2013).
9. Hunt, B. et al. Massive Dirac fermions and Hofstadter butterfly in a van der Waals heterostructure. *Science* **340**, 1427–1430 (2013).
10. Woods, C. R. et al. Commensurate–incommensurate transition in graphene on hexagonal boron nitride. *Nat. Phys.* **10**, 451–456 (2014).
11. Gorbachev, R. V. et al. Detecting topological currents in graphene superlattices. *Science* **346**, 448–451 (2014).
12. Wang, L. et al. Evidence for a fractional fractal quantum Hall effect in graphene superlattices. *Science* **350**, 1231–1234 (2015).
13. Wang, E. et al. Gaps induced by inversion symmetry breaking and second-generation Dirac cones in graphene/hexagonal boron nitride. *Nat. Phys.* **12**, 1111–1115 (2016).
14. Spanton, E. M. et al. Observation of fractional Chern insulators in a van der Waals heterostructure. *Science* **360**, 62–66 (2018).
15. Dean, C. R. et al. Boron nitride substrates for high-quality graphene electronics. *Nat. Nanotech.* **5**, 722–726 (2010).
16. Park, C.-H., Yang, L., Son, Y.-W., Cohen, M. L. & Louie, S. G. New generation of massless Dirac fermions in graphene under external periodic potentials. *Phys. Rev. Lett.* **101**, 126804 (2008).
17. Chen, G. et al. Emergence of tertiary Dirac points in graphene moiré superlattices. *Nano Lett.* **17**, 3576–3581 (2017).
18. Kim, K. et al. Van der Waals heterostructures with high accuracy rotational alignment. *Nano Lett.* **16**, 1989–1995 (2016).
19. Woods, C. R. et al. Macroscopic self-reorientation of interacting two-dimensional crystals. *Nat. Commun.* **7**, 10800 (2016).
20. Chari, T., Ribeiro-Palau, R., Dean, C. R. & Shepard, K. Resistivity of rotated graphite–graphene contacts. *Nano Lett.* **16**, 4477–4482 (2016).
21. Koren, E. et al. Coherent commensurate electronic states at the interface between misoriented graphene layers. *Nat. Nanotech.* **11**, 752–757 (2016).
22. Solozhenko, V. L., Will, G. & Elf, F. Isothermal compression of hexagonal grpahite-like boron nitride up to 12 GPa. *Solid State Commun.* **96**, 1–3 (1995).
23. Chen, Y. et al. Pressurizing field-effect transistors of few-layer MoS_2 in a diamond anvil cell. *Nano Lett.* **17**, 194–199 (2017).
24. Chen, Z.-G. et al. Observation of an intrinsic bandgap and Landau level renormalization in graphene/boron-nitride heterostructures. *Nat. Commun.* **5**, 4461 (2014).
25. Song, J. C. W., Shytov, A. V. & Levitov, L. S. Electron interactions and gap opening in graphene superlattices. *Phys. Rev. Lett.* **111**, 266801 (2013).
26. Bokdam, M., Amlaki, T., Brocks, G. & Kelly, P. J. Band gaps in incommensurable graphene on hexagonal boron nitride. *Phys. Rev. B* **89**, 201404(R) (2014).
27. Moon, P. & Koshino, M. Electronic properties of graphene/hexagonal-boron-nitride moiré superlattice. *Phys. Rev. B* **90**, 155406 (2014).
28. Wallbank, J. R., Mucha-Kruczynski, M., Chen, X. & Fal'ko, V. I. Moiré superlattice effects in graphene/boron-nitride van der Waals heterostructures. *Ann. Phys.* **527**, 359–376 (2015).
29. Jung, J., DaSilva, A. M., MacDonald, A. H. & Adam, S. Origin of band gaps in graphene on hexagonal boron nitride. *Nat. Commun.* **6**, 6308 (2015).
30. San-Jose, P., Gutiérrez-Rubio, A., Sturla, M. & Guinea, F. Spontaneous strains and gap in graphene on boron nitride. *Phys. Rev. B* **90**, 075428 (2014).
31. Slotman, G. et al. Effect of structural relaxation on the electronic structure of graphene on hexagonal boron nitride. *Phys. Rev. Lett.* **115**, 186801 (2015).
32. Jung, J. et al. Moiré band model and band gaps of graphene on hexagonal boron nitride. *Phys. Rev. B* **96**, 085442 (2017).
33. Yankowitz, M., Watanabe, K., Taniguchi, T., San-Jose, P. & LeRoy, B. J. Pressure-induced commensurate stacking of graphene on boron nitride. *Nat. Commun.* **7**, 13168 (2016).

Acknowledgements We thank P. San-Jose, J. Song, A. Shytov, L. Levitov, J. Wallbank and P. Moon for theoretical discussions. This work was supported by the National Science Foundation (NSF) (DMR-1462383). C.R.D. acknowledges partial support from the David and Lucille Packard foundation. Development of the device concept and fabrication process was partially supported by the NSF MRSEC program through Columbia in the Center for Precision Assembly of Superstratic and Superatomic Solids (DMR-1420634). We acknowledge S. Tozer for use of his 16 T PPMS which is partially supported as part of the Center for Actinide Science and Technology (CAST), an Energy Frontier Research Center (EFRC) funded by the Department of Energy, Office of Science, Basic Energy Sciences under award no. DE-SC0016568. A portion of this work was performed at the National High Magnetic Field Laboratory, which is supported by NSF Cooperative Agreement no. DMR-1157490, the State of Florida and the US Department of Energy and additionally provided support for pressure cell development through User Collaboration Grant Program (UCGP) funding. J.J. and N.L. were supported by the Korean NRF through grant NRF-2016R1A2B4010105 and Korean Research Fellowship grant NRF-2016H1D3A1023826, and B.L.C. was supported by grant NRF-2017R1D1A1B03035932. E.L. and S.A. are supported by the National Research Foundation of Singapore under its Fellowship program (NRF-NRFF2012-01) and the Singapore Ministry of Education AcRF Tier 2 (MOE2017-T2-2-140). K.W. and T.T. acknowledge support from the Elemental Strategy Initiative conducted by the MEXT, Japan, and JSPS KAKENHI grant no. JP15K21722.

Author Contributions M.Y. and C.R.D. conceived the experiment. M.Y. fabricated the samples and analysed the data. M.Y. and D.G. performed the experiments. J.J., E.L. and S.A. developed the theory. N.L. and B.L.C. calculated the ab initio potentials. K.W. and T.T. grew the hBN crystals. C.R.D. advised on the experiments. All authors participated in writing the paper.

Competing interests The authors declare no competing interests.

Additional information
Extended data is available for this paper at https://doi.org/10.1038/s41586-018-0107-1.
Supplementary information is available for this paper at https://doi.org/10.1038/s41586-018-0107-1.
Reprints and permissions information is available at http://www.nature.com/reprints.
Correspondence and requests for materials should be addressed to C.R.D.
Publisher's note: Springer Nature remains neutral with regard to jurisdictional claims in published maps and institutional affiliations.

METHODS

Device structure and application of pressure. All devices in this study consist of monolayer graphene encapsulated between two layers of BN. The BN layers were 20–60 nm thick, although our results did not depend on this in any important way. The encapsulated stack sits on a flake of graphite that acts as a local back gate, and the entire stack rests on a Si/SiO$_2$ wafer (Fig. 1a). Extended Data Fig. 1a shows an image of a completed heterostructure on a transfer slide. For aligned samples, the graphene (outlined with a dashed white line) was either intentionally aligned optically to one of the BN layers using crystalline edges of the flakes[7] or incidentally through self-rotation to an aligned position, which has lowest stacking potential energy, upon heating during the transfer process[12,19]. The final device was partially etched into a Hall bar geometry, leaving some of the bottom BN unetched to prevent the metal contacts from shorting to the graphite gate (Extended Data Fig. 1b). We make one-dimensional electrical contact using standard reactive ion etching and electron-beam patterning and deposition techniques[3]. The Hall bar was intentionally kept small (approximately 6 μm by 2 μm) to keep the pressure as uniform as possible across the entire device. The Si/SiO$_2$ substrate is diced to approximately 2 mm by 2 mm to fit into the inner bore of the pressure cell (Extended Data Fig. 1c).

To prepare the pressure cell, a clean metal stage (Extended Data Fig. 1d) is threaded with insulated copper 75 μm wires with tinned ends, which are epoxied in place using Stycast 2850 FT using 24LV catalyst (Extended Data Fig. 1e). A ruby crystal is glued to the tip of a thin optical fibre that is fixed in place by the wires for in situ pressure calibration. The sample is then glued above the fibre (Extended Data Fig. 1f). Flexible 15 μm Pt wires are soldered to the copper wires and affixed by hand to the gold sample contacts using Dupont 4929 N silver paste (Extended Data Fig. 1g). Next, a Teflon cup is filled with the pressure medium (Daphne 7373 or 7474 oil[34,35]) and carefully fitted over the sample and onto the stage (Extended Data Fig. 1h). The sample is then completely encapsulated in oil. For the special case of vacuum measurements (0 GPa), no oil is loaded into the Teflon cup. The stage/Teflon cup is then fitted into the inner bore of a piston cylinder cell (Extended Data Fig. 1i) and a hydraulic press is used to compress the top of the Teflon cup (Extended Data Fig. 1j), which is held in place by a locking nut. The cell is then affixed to the end of a probe (Extended Data Fig. 1k) for low-temperature, high-field measurements. The pressure was determined by measuring the fluorescence response of the ruby crystal at both room temperature and low temperature[36,37]. Changing the pressure requires warming the cell to room temperature, adding or removing load with the hydraulic press, and re-cooling the cell. Although the pressure in the cell is uniform, the Young's modulus in the the out-of-plane stacking direction (c axis) of vdW crystals is typically a few orders of magnitude smaller than in-plane[38]; hence the pressure primarily results in a c-axis compression.

Although the oil does not noticeably influence the electronic properties of the device, special care must be taken to account for its presence during measurements. The oil freezes at around 200 K as it is cooled at ambient pressure, and the freezing point moves to higher temperatures at higher starting loads. The pressure in the cell also drops as the oil cools inside the cell, with a larger relative drop in pressure at smaller initial loads. For example, a starting load below about 0.3 GPa at room temperature will result in nearly ambient conditions at low temperature, whereas at pressures above 2 GPa there is virtually no change between the room-temperature and low-temperature pressures. We have found that the primary consequence of this effect is that starting at room-temperature loads of roughly 0.5 GPa or less is dangerous for the device, as the stack is typically torn when the oil freezes below these pressures. However, above these pressures the devices always survive the cooling, and we have not noticed any effect of the oil freezing in transport measurements. Finally, special care is taken to account for the large thermal load of the pressure cell when performing temperature sweeps to measure bandgaps. The temperature is swept slowly to keep the sample as close to equilibrium as possible, ideally at 0.5 K min^{-1}, and no faster than 1.5 K min^{-1}.

Apart from the change in PDP resistance, we typically do not observe much modification of the electronic response of our devices with pressure. For device P2 (results shown in Fig. 1b), an increase of 15–25 Ω is observed at high density under pressure, although this is not always the case. For example, Extended Data Fig. 2 shows similar transport measurements for device P3, in which we observe virtually no change in the device resistivity for hole carriers, and a decrease in the resistivity for electron carriers. In any case, the change in high-density response is always very small compared with the effect of pressure at the PDP.

Extraction of bandgaps and capacitance. We extract the bandgaps Δ of the PDP and SDP at each pressure according to the thermally activated response where $\sigma_{\mathrm{PDP}}(T) \propto \mathrm{e}^{-\Delta/(2kT)}$, where k is the Boltzmann constant. The error bars on the gap values in Fig. 3b reflect the uncertainty in determining the temperature range over which the Arrhenius plot shows a linear response. The upper and lower error boundaries correspond to the magnitude of the gap sizes extracted when fitting a line to the minimum and maximum temperature ranges over which the dispersion in Fig. 3a could be reasonably judged as linear. The error arising from the uncertainty determining the extraction range is much larger than the standard error in any individual linear regression. Figure 3a shows this fit for the PDP in device P1 as a function of pressure, and Extended Data Fig. 3 similarly shows this fit for the valence-band SDP, demonstrating that the latter gap does not change appreciably with pressure.

To find the gate capacitance, we extract $n(V_{\mathrm{g}})$ for each pressure through either the dispersion of the quantum Hall states in high magnetic field as $n = \nu eB/h$, where ν is the filling factor (Fig. 2a), or from the low-field Hall resistance R_{xy} before the onset of strong Shubnikov–de Haas oscillations as $n = B/(eR_{xy})$ (Fig. 2b). Quantum Hall states move symmetrically closer to the PDP with increasing pressure, and the slope of the Hall resistance decreases with pressure, both implying a growing $n(V_{\mathrm{g}})$ with increasing pressure. In Fig. 2c, C_{g} is normalized to its measured value at 0 GPa to account for the different thicknesses of the bottom BN layers across the different devices. Additionally, the ab initio value of ε at 0 GPa is normalized to match the average experimental value of about 3. Our ab initio simulations also confirm that the BN dielectric constant should grow with pressure, although the effect is predicted to be a few times smaller (green curve in bottom inset), probably owing to the absence of many-body and excitonic effects in our calculations (see Supplementary Information for further discussion).

Gap evolution in other devices. We have measured a total of six devices as a function of pressure. Extended Data Fig. 4a plots the gap of the PDP, where the data from device P1 are copied from the main text. Error bars are left off for clarity, but are similar in magnitude to those in Fig. 3b. All devices except P1 are misaligned more than about 2° from both BNs, as we do not observe any SDPs within the experimentally accessible carrier density ranges (therefore the exact rotation angle is unknown). Previous work has demonstrated that devices with misalignment angles as large as about 5° can exhibit bandgaps in transport[9]. In that study, the misalignment angle was determined by scanning tunnelling topography measurements, but this is not possible in our devices owing to the presence of the encapsulating top BN layer. Nevertheless, some of these devices (P3 and P4) show clear activation gaps, with insulating behaviour at low temperatures and a decrease of the device conductivity by nearly an order of magnitude in the thermally activated regime at high temperatures (Extended Data Fig. 5c, d). Two of the devices (P2 and P5) only exhibit activated behaviour over a much smaller range, but we can nevertheless perform the gap fit over the regime that is activated, with the understanding that this number may not be an accurate measure of the bandgap. These gaps are denoted with triangle markers on the plot in Extended Data Fig. 4a. Strikingly, in every device studied the gap grows with increasing pressure, and the magnitude of the gap enhancement seems to scale roughly with the magnitude of the gap at 0 GPa. This is consistent with our proposed model in which the gap depends on the interlayer electronic coupling between the graphene and BN, as well as lattice deformations resulting from structural relaxation of the graphene to minimize the stacking energy, the latter of which should diminish quickly with increasing misalignment angle. Although we expect that the misalignment angle in these devices is larger for devices with smaller gaps at 0 GPa, this remains an open question owing to our inability to directly probe the angular misalignments with each BN.

We also measured a second aligned sample (device P6), with an estimated misalignment angle of about 0.1°. This device was considerably more disordered than all the other devices in this study, and as a result the onset of the variable-range hopping regime was at higher temperature. Consequentially, the thermally activated regime spanned only a small range of temperature, and therefore the gap extraction is more ambiguous than for the other aligned device (P1). Nevertheless, the Δ_{p} showed a clear enhancement with pressure, whereas Δ_{s} seemed relatively insensitive to pressure (Extended Data Fig. 4b). This behaviour is consistent with the clean aligned device (P1) presented in the main text, providing further evidence of the fundamental difference between the primary and secondary Dirac points.

The enhancement of the bandgap does not depend on the history of the pressure to which the device has been exposed, but rather responds directly to the pressure the device is under at the time of measurement. To illustrate this, Extended Data Fig. 4a annotates the order in which the gaps were acquired. In no case does the measured gap fall out of the anticipated sequence. We have also examined the PDP conductivity at the lowest temperatures measured, but we find that this is not a good measure of the bandgap as it is additionally influenced by the effects of residual disorder in the variable-range hopping regime[9]. Extended Data Fig. 5 tracks the PDP conductivity across all measured devices below 2 K. Typically the resistance of the PDP is higher at low temperature for higher pressures, however this is not always the case. For devices P1 and P3, the low-temperature conductivity becomes out of sequence upon unloading pressure, or in reloading pressure after previously pressure cycling and returning to 0 GPa (see the annotations in Extended Data Fig. 4a for the order of curve acquisition). Even in device P4, for which the pressure was loaded up uniformly, the low-temperature conductivity still depends non-monotonically on pressure. This suggests that small changes in the magnitude of disorder in the device and potentially even the details of its microscopic organization can ultimately influence how insulating the device becomes. However, no matter how the PDP conductivity behaves at low temperature, the bandgap is always enhanced by pressure, suggesting that the gap enhancement is a robust property of the heterostructure and depends most critically on the interlayer interaction strength between the graphene and the BN rather than small changes in device disorder.

Effects of pressure in the quantum Hall regime. The disorder in these devices can also be characterized by considering the density n necessary to switch the Hall resistance R_{xy} from positive to negative (Extended Data Fig. 6a), as this gives a measure of the effective magnitude of the electron–hole puddles in the bulk. Extended Data Fig. 6b shows that the device disorder is not strongly dependent on pressure, growing by less than the extraction uncertainty over the applied pressure range. Curiously, pressure serves to qualitatively improve the quantum Hall response at high magnetic field. Extended Data Fig. 6c shows one such example, where both integer and fractional quantum Hall states develop more clearly under pressure. This effect is observed in every device examined. Surprisingly, we find that this improvement persists even after the pressure is released (Extended Data Fig. 6d), suggesting that this improvement is an irreversible effect. At present, we may only speculate as to the nature of this effect.

First, it is important to note that despite the high electronic quality of the devices, only the main sequence of IQH gaps, at $\nu = -2, -6, -10$ and so on, are typically fully developed in initial measurements in vacuum, with the symmetry-broken gaps still developing (Extended Data Fig. 6d). The poor development of the QHE despite the high mobility is symptomatic of the device geometry used here (Extended Data Fig. 1b), where the metal contacts sit above the graphite gate. Although the reason for this is currently not well understood, the situation may be analogous to previous observations in GaAs, in which a partial reduction of the carrier concentration in the graphene just in front of the contacts can lead to a depletion region along the boundary, which may impede the ability to observe well-developed quantum Hall plateaus[39]. This problem has been addressed previously by leaving Si-gated regions of the graphene to act as electrical contacts to the Hall bar, where the density at the boundary can vary more smoothly[40]. However, the devices in this study were intentionally kept small to ensure the pressure was as uniform as possible across the device, and so this geometry was not used.

Applying pressure may, for instance, provide a way to reduce this depletion region at the contacts, permitting better coupling to the quantum Hall edge modes. This could arise because of self-cleaning of contaminants along the contact boundaries, or if the metal making edge contact to the graphene forms a better bond to the graphene edge and lowers the work function mismatch at the boundary. Both of these effects could in principle persist even after the pressure is released. We find that the contact resistance is not noticeably modified by pressure at $B = 0$ T (Fig. 1b), pointing to an improvement arising from the detailed electrostatics at the contact barrier in high magnetic field, or to a reduction of non-local contamination which may be most relevant in the quantum Hall regime. Further study is necessary to understand the exact nature of this effect.

Finally, we examine the effects of pressure on the Hofstadter butterfly spectrum of the aligned device P1. Extended Data Fig. 7 shows the high-field response at ambient conditions (Extended Data Fig. 7a) and at 2.3 GPa (Extended Data Fig. 7b). As pressure enhances the coupling to the MSL, it should consequentially modify the relative strength of magnetotransport features arising from the secondary Dirac cones. We observe that under pressure the longitudinal magnetoresistance becomes larger for features arising from the valence band SDP, in qualitative agreement with the expectation of a stronger MSL. However, this must be deconvolved with the overall change in the quantum Hall behaviour with pressure, and a full investigation of the dependence of integer and fractional quantum Hall gaps on pressure is outside the scope of this work.

Theoretical model. Graphene and BN are two-dimensional materials with hexagonal crystal structures, but with different lattice constants. When graphene is deposited on a BN substrate with near-perfect alignment (small twist angles), the slight lattice mismatch ($\varepsilon \approx 1.7\%$) leads to the formation of a moiré structure which is characterized by a wavelength that is one to two orders of magnitude larger than the graphene unit cell. As a consequence, the dynamics of the low-energy Dirac electrons of graphene are governed by the corresponding long-wavelength component of the electronic couplings. Similarly, the interlayer potentials and deformations in graphene/BN are also largely characterized by this long-wavelength theory. The dominant contributions are captured by the first harmonics of the moiré structure[28,29,41] characterized by a set of vectors $\boldsymbol{G}_m$ that are related to the original graphene lattice vectors $\boldsymbol{g}_m$ by

$$\boldsymbol{g}_m = \hat{\boldsymbol{R}}_{2\pi(m-1)/6}(0, g), \quad \boldsymbol{G}_m = [(1+\varepsilon) - \hat{\boldsymbol{R}}_\theta]\boldsymbol{g}_m \approx \varepsilon \boldsymbol{g}_m - \theta \hat{\boldsymbol{z}} \times \boldsymbol{g}_m \qquad (1)$$

where $m \in \{1, 2, \ldots, 6\}$, $\hat{\boldsymbol{R}}_\theta$ denotes a rotation by θ, and $g = 4\pi/(3a)$ is the length of graphene lattice vectors with $a \approx 1.42$ Å the carbon–carbon distance. The approximate sign indicates the approximation within the small twist angle limit ($\theta \ll 1$). We show in Supplementary Information that $\boldsymbol{G}_m$ defines the moiré Brillouin zone, whose lateral dimension is scaled by $\tilde{\varepsilon} = \sqrt{\varepsilon^2 + \theta^2}$ with respect to the graphene Brillouin zone and is less than about 5% for twist angles θ of less than about 2°. In the graphene/BN system which possesses triangular symmetry, we can define two periodic functions within the first harmonics: $f_1(\boldsymbol{r}) = \sum_m \exp(i\boldsymbol{G}_m \cdot \boldsymbol{r})$ which satisfies inversion and hexagonal symmetries, and $f_2(\boldsymbol{r}) = -i\sum_m (-1)^m \exp(i\boldsymbol{G}_m \cdot \boldsymbol{r})$ which is asymmetric under inversion.

The low-energy Hamiltonian for the coupled graphene on BN system can be conveniently decomposed into a basis of $f_1(\boldsymbol{r})$ and $f_2(\boldsymbol{r})$. Consistent with previous results[32], we choose a reference frame in which the inversion-asymmetric couplings are an order of magnitude larger than the inversion-symmetric electronic couplings, which allows us to simplify the theoretical analysis considerably and obtain closed-form expressions for the primary and secondary gaps. Here we provide a qualitative discussion of the primary and secondary gaps, leaving the detailed analysis for Supplementary Information.

Both gaps have an exponential prefactor $e^{-\beta(z_0 - z_r)}$, which results in an increase in the gap arising from the increased coupling between the graphene and BN when the two layers are driven closer together under pressure. For Δ_p, we find that this exponential prefactor is modified by two terms. The first depends only on the corrugations and to leading order is given by the symmetric component of the out-of-plane deformations. The second term, proportional to the elastic deformability of the graphene, depends on both in-plane and out-of-plane deformations, but for realistic parameters depends only on the symmetric component of the deformations. As a result, to leading order Δ_p is determined by the symmetric in-plane and out-of-plane deformations and vanishes in the case of rigid graphene. In contrast, Δ_s is finite even for the rigid case without any deformations, and has additional terms arising from the electrostatic potentials and pseudomagnetic fields of the moiré structure which are not proportional to the exponential prefactor and provide a negative contribution to the magnitude of the gap. The experimental observation that $\Delta_\mathrm{p} > \Delta_\mathrm{s}$ implies that these negative terms are of comparable magnitude to the terms that scale exponentially with interlayer separation. Furthermore, Δ_s is controlled by both the symmetric and asymmetric components of the deformation, and to remain constant under pressure the difference between the symmetric and asymmetric deformations must increase with pressure. Additional analysis is provided in Supplementary Information.

Data availability. The data presented in the figures and that support the other findings of this study are available from the corresponding author on reasonable request.

34. Murata, K., Yoshina, H., Yadav, H. O., Honda, Y. & Shirakawa, N. Pt resistor thermometry and pressure calibration in a clamped pressure cell with the medium, daphne 7373. *Rev. Sci. Instrum.* **68**, 2490–2493 (1997).
35. Murata, K. et al. Pressure transmitting medium Daphne 7474 solidifying at 3.7 gpa at room temperature. *Rev. Sci. Instrum.* **79**, 085101 (2008).
36. Piermarini, G. J., Block, S. & Barnett, J. D. Hydrostatic limits in liquids and solids to 100 kbar. *J. Appl. Phys.* **44**, 5377–5382 (1973).
37. Ragan, D. D., Gustavsen, R. & Schiferl, D. Calibration of the ruby R_1 and R_2 fluorescence shifts as a function of temperature from 0 to 600 K. *J. Appl. Phys.* **72**, 5539–5544 (1992).
38. Blakslee, O. L., Proctor, D. G., Seldin, E. J., Spence, G. B. & Weng, T. Elastic constants of compression-annealed pyrolytic grpahite. *J. Appl. Phys.* **41**, 3373–3382 (1970).
39. Weis, J. & von Klitzing, K. Metrology and microscopic picture of the integer quantum Hall effect. *Philos. Trans. R. Soc. Lond. A* **369**, 3954–3974 (2011).
40. Maher, P. et al. Tunable fractional quantum hall phases in bilayer graphene. *Science* **345**, 61–64 (2014).
41. Bistritzer, R. & MacDonald, A. H. Moiré bands in twisted double-layer graphene. *Proc. Natl Acad. Sci. USA* **108**, 12233–12237 (2011).

Extended Data Fig. 1 | Pictures of the set-up for pressure experiments. **a**, Graphene (outlined in white dashed line) is encapsulated between BN and placed on a graphite back gate. **b**, The device is shaped into a Hall bar and contacted for electrical measurements. **c**, The Si wafer is diced to approximate dimensions of 2 mm × 2 mm. **d**, A new pressure cell stage. **e**, The stage is threaded with wires which are epoxied in place. **f**, The sample is glued to the top of the stage. **g**, Wires are connected to the device electrodes by hand using silver paste. **h**, A Teflon cup is filled with oil and fitted over the sample and onto the stage. **i**, The sample is placed into a pressure cell. **j**, Pressure is loaded using a hydraulic press. **k**, The loaded pressure cell is attached to a probe for low-temperature magnetotransport measurements. See Methods for complete experimental details. The scale bars for **a** and **b** are 25 μm, and the scale bar for **c** is 2 mm.

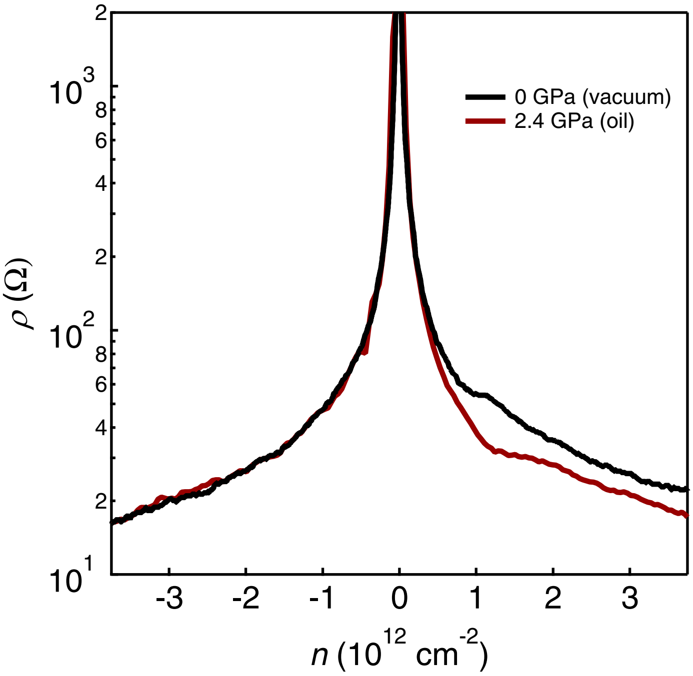

Extended Data Fig. 2 | Resistivity of device P3 at $B = 0$ T and $T = 2$ K. For the application of high pressure in this device, we observe virtually no change in the device resistivity for hole carriers, and a decrease in the resistivity for electron carriers.

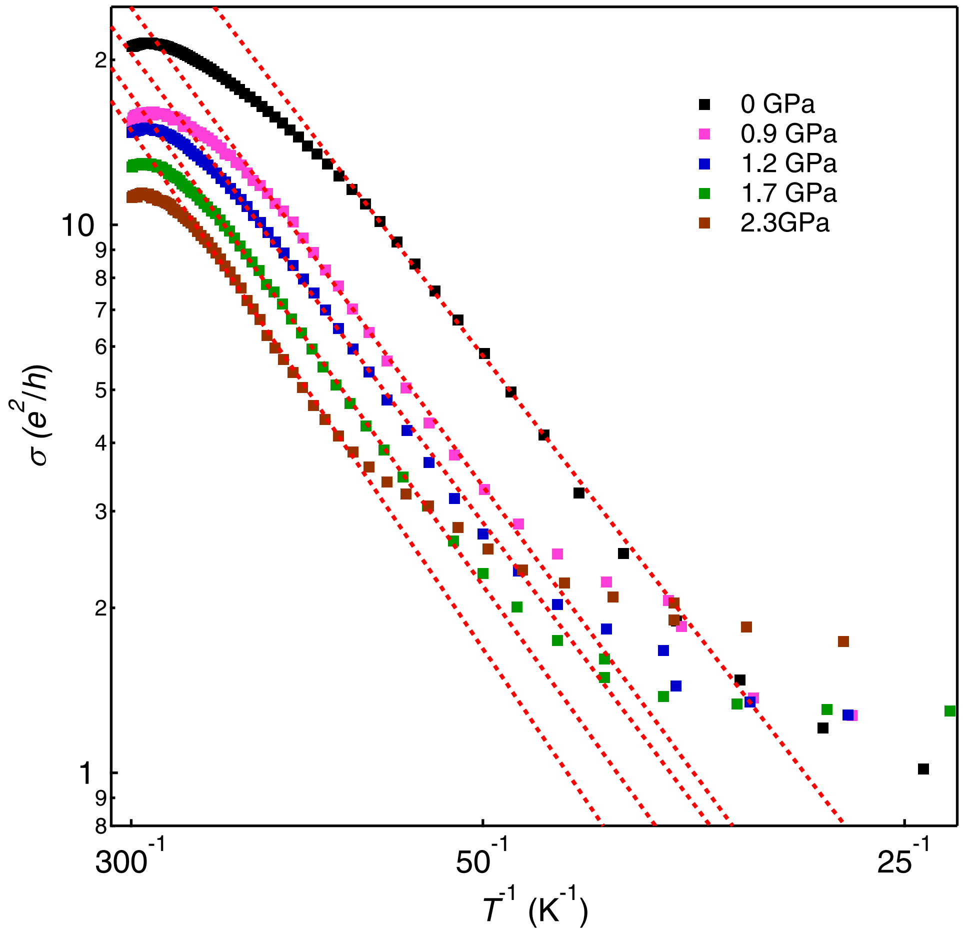

Extended Data Fig. 3 | Arrhenius plot for the SDP in device P1. The gap exhibits virtually no dependence on pressure.

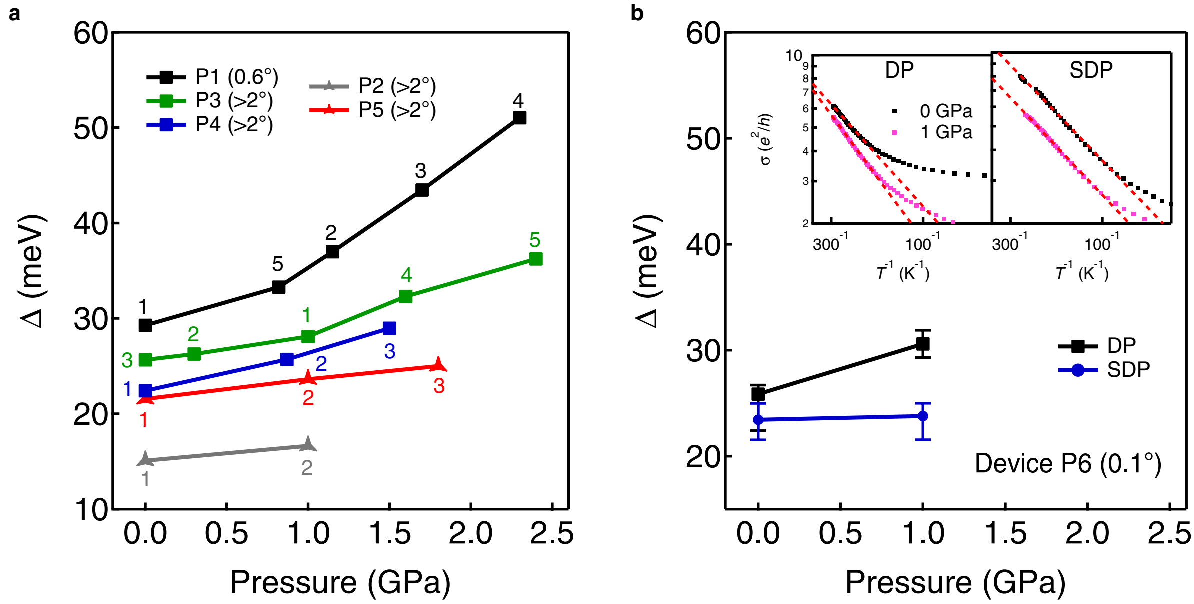

Extended Data Fig. 4 | Bandgaps as a function of pressure for all devices studied. a, Devices with square markers exhibit thermally activated behaviour over roughly an order of magnitude change in resistance. Devices with triangle markers exhibit thermally activated behaviour over a smaller range. The numbered labels represent the order in which the gaps were acquired. The gap magnitude depends only on the pressure the device is under at the time of measurement, and not on the history of the pressure that has been previously applied. Error bars in the gap fitting arising from the uncertainty identifying the thermally activated regime have been omitted for clarity, but are all less than 2.5 meV. **b**, Gap dependence in a second aligned device (P6), with misalignment of about 0.1°. This device also exhibits a growing Δ_p and constant Δ_s, but is much more disordered than device P1. Inset: Arrhenius plots for the PDP (left) and SDP (right) at 0 GPa and 1 GPa.

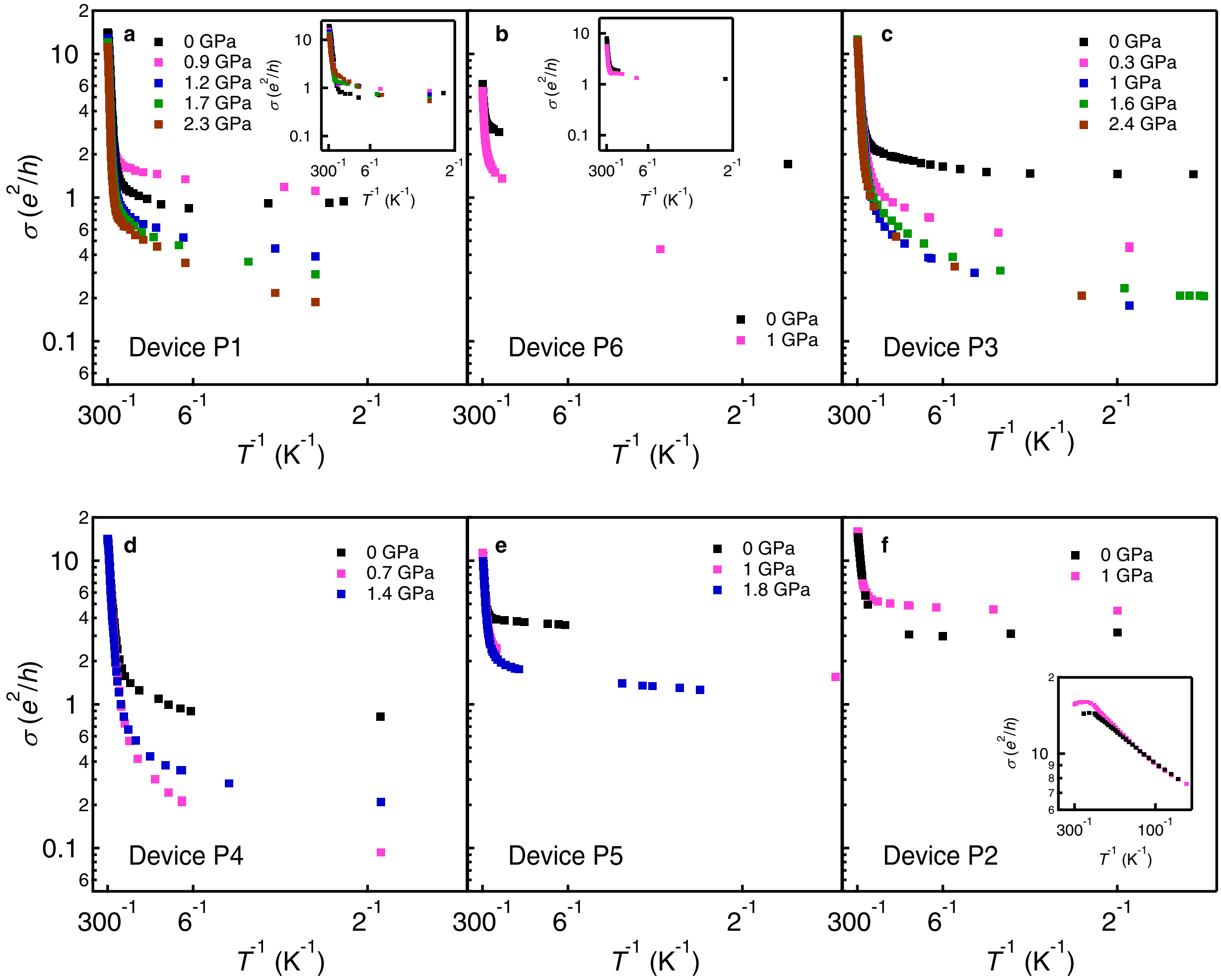

Extended Data Fig. 5 | Conductivity of the PDP over the full temperature range at various pressures for all devices studied. **a**, Device P1 is the aligned device discussed in the main text. Inset, conductivity of the SDP. **b**, Device P6 is a second aligned device, but is more highly disordered and therefore less resistive at low temperature. Inset, conductivity of the SDP. **c**–**f**, The remaining devices do not exhibit SDPs, and therefore the alignment to the BN layers is unknown. However, the devices in **c** and **d** still exhibit thermally activated behaviour over roughly an order of magnitude change in resistance, suggesting they are nearly aligned to a BN. The devices in **e** and **f** have a much smaller thermally activated regime. Pressure tends to have a smaller effect on the PDP conductivity for devices that are less resistive at 0 GPa. The inset in **f** shows the high-temperature response, demonstrating the weak effect of pressure in the thermally activated regime for the least resistive device. In **a**–**f**, although the PDP generally grows more insulating with higher pressure at low temperatures, this is not universally true, suggesting that the details of the low-temperature resistance depends more critically on the exact nature of disorder in the device. Devices are ordered by decreasing gap size as measured in the thermally activated regime.

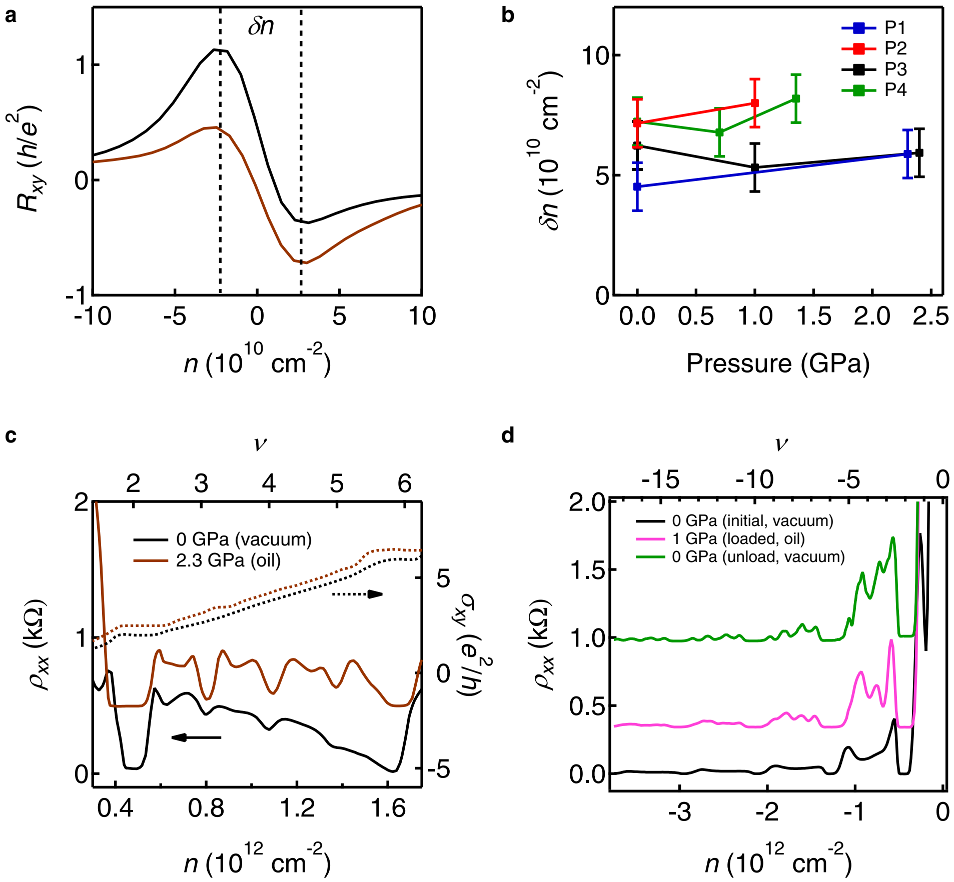

Extended Data Fig. 6 | Disorder and the quantum Hall effect. **a**, Device disorder δn is measured as the n necessary to dope between the maximum and minimum R_{xy}, averaged over $B = 0.25$ T to 0.75 T. **b**, Density fluctuations as a function of pressure across different devices. The error bars denote the uncertainty in picking the peak positions of R_{xy}. **c**, ρ_{xx} (solid lines, left axis) and σ_{xy} (dotted lines, right axis) of device P1 at $B = 12.5$ T. Symmetry-broken integer quantum Hall states become much more clearly developed with pressure, and fractional quantum Hall states begin to emerge as well. Both are offset for clarity. **d**, ρ_{xx} of device P2 at $B = 9$ T, similarly showing an improvement in the quantum Hall response. Surprisingly, the improvement persists even after the pressure is released back to vacuum and the device is cleaned in solvents (green curve). Curves are vertically offset for clarity.

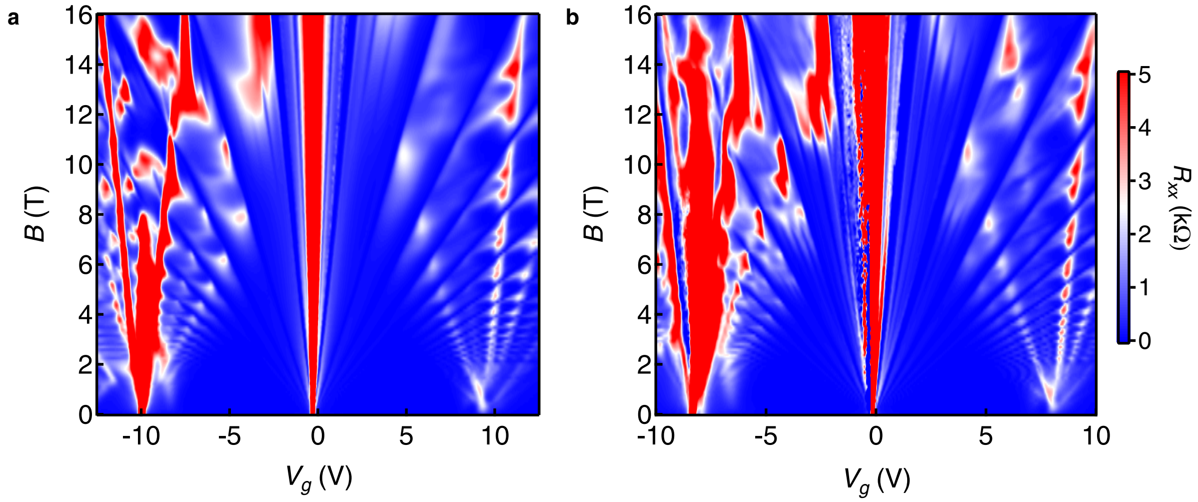

Extended Data Fig. 7 | Hofstadter butterfly as a function of pressure in device P1. Magnetotransport data acquired at $T = 2$ K and a pressure of: **a**, 0 GPa; **b**, 2.3 GPa.